Measurement 235 (2024) 115020

Contents lists available at ScienceDirect

Measurement

journal homepage: www.elsevier.com/locate/measurement

Fireball symmetry and its influence on perspective error from thermography data

Colton Cagle, Michelle Pantoya *

Mechanical Engineering Department, Texas Tech University, Lubbock, TX USA

ARTICLE INFO

Keywords:
Thermography
Optical Pyrometry
Flame Symmetry
Perspective Error
Reactive Materials
Ballistics

ABSTRACT

Thermography uses high-speed color cameras to perform two-color pyrometry for measuring spatially resolved surface temperatures of condensed phases. One application is to investigate the thermal evolution of particles within fireballs, but data analysis is affected by emissivity and optical density. Fireball dynamics exhibit large variations in both properties across space and time, while diagnostics measure the line-of-sight radius of a maturing fireball, raising the question: does thermography accurately represent temperature distributions regardless of spatial perspective? Here, fireballs are observed at two 90° perspectives. Every frame of data is categorized based on symmetry, then compared using the median temperature difference. Symmetric flame profiles show higher congruity in global median temperature, whereas asymmetric flames produce varying optical density profiles leading to larger differences between perspectives. Methods to correct perspective errors are discussed.

1. Introduction

Imaging diagnostics such as thermography are an integral tool of modern combustion research [1–3]. Thermography uses a camera sensor to isolate wavelengths of light then processes data using ratio pyrometry on a pixel-by-pixel basis [2]. The array of pixelated data allows high-density surface mapping of temperature, producing time-resolved temperature profiles for the imaged field of view. Recent advances in combustion models employ machine learning (ML) and neural network (NN) techniques [4], such that diagnostics that provide large datasets of spatially and temporally resolved thermal and fluid dynamics are particularly valuable for model validation and training. However, uncertainties and errors in thermography can be large, limiting the utility of this technique [1,2]. Dynamic reactive events face particular scrutiny due to the numerous assumptions necessary for data processing [3]. As such, measured temperature is more accurately an apparent temperature that is inseparable from the analysis and experimental configuration under study. Nevertheless, thermographic data is still valuable when appropriately deployed and uncertainties defined [5]. Therefore, to facilitate the implementation of thermography as a combustion diagnostic, a hypothesis is tested that a single perspective may not accurately characterize data from a combustion event. The objective of this study is to quantify the influence of perspective on thermographic data captured during impact initiated reactive material (RM) combustion.

Imaging diagnostics are limited by the interplay between 3-D projections of reality onto a 2-D plane, sometimes referred to as perspective projection [6] and illustrated in Fig. 1. Spherically symmetric objects may be imaged at any position and angle yet still produce an identical profile in the imaging plane. If the object is transformed into a ring, the profile projected onto the imaging plane now greatly depends on relative positions in space, as shown in Fig. 1. The appearance variations illustrated in Fig. 1 are called perspective error [6].

Perspective error does not necessarily indicate an issue with collected data, only that the data provide limited information. Perspective error has been successfully addressed in fields such as photographic reconstruction, medical technology, and modelling through the 3-D reconstruction of complex objects from 2-D images [7–9]. However, the effect of perspective on data from combustion studies has not been investigated, to the authors awareness.

This study on perspective error will focus on Reactive Material (RM) combustion. RMs are mixtures of solid fuels (e.g., aluminum (Al), zirconium (Zr)) and may also include solid oxidizers (e.g., molybdenum trioxide (MoO_3)). Reactions are multi-phase and generate condensed phase particles (e.g., alumina (Al_2O_3)) at elevated temperatures (i.e., > 2000 K) [10]. In this study, ignition is triggered by launching RM

* Corresponding author.
E-mail address: michelle.pantoya@ttu.edu (M. Pantoya).

https://doi.org/10.1016/j.measurement.2024.115020
Received 6 January 2024; Received in revised form 27 May 2024; Accepted 28 May 2024
Available online 28 May 2024
0263-2241/

powder consolidated into projectiles at high velocities (i.e., $>$ 1000 m/s) and observing impact, fragmentation, and reaction inside a test chamber. Croessmann et al. [11] showed for RM projectiles, energy release is dominated by radiant energy emission and chemical energy conversion occurs primarily in the condensed phase (i.e., $>$ 50 %). Thermography and pyrometry measurements are primarily condensed phase measurements because condensed phase emissions overpower gaseous emissions at relevant conditions [12]. Therefore, RM combustion is conducive to pyrometry diagnostics and a good subject for this study on perspective error.

Perspective errors will be discussed as an effect of either natural flame asymmetries during reaction or optical density variations within the flame profile. Perspective error originating from flame asymmetry is a natural difference in the observed profile of the flame. Perspective error originating from optical density is interpreted as a flame of uniform temperature in the shape of a long cylinder being imaged both on and off-axis. When analyzed, on-axis measurements are notably different than off-axis. This perspective error is mainly caused by the incorrect application of the wavelength (λ) dependent emissivity (ε) approximation function (i.e., $\boldsymbol{\varepsilon} = 1$, $\boldsymbol{\varepsilon} = \frac{1}{\lambda}$, and $\boldsymbol{\varepsilon} = \frac{1}{\lambda^2}$) based on varying optical density of the flame profile observed. It is noted that further theoretical development on the spectral-directional dependence of emissivity could guide experimentalists by advancing methods used to process emission data and more accurately unravel thermal flame behavior. However, the current work applies standard pyrometry data processing methods with focus on temperature inference as a function of perspective thereby resulting in perspective error.

To isolate the significance of perspective error, this study intentionally examined an array of different RM formulations and impact ignition configurations to produce varying flame profiles that could be imaged from multiple perspectives simultaneously. Every still frame flame profile is categorized based on flame symmetry and allow comparisons between idealized flame expansion (i.e., symmetric behavior) versus highly stochastic (i.e., asymmetric behavior) systems. Data as a function of perspective are quantified and provide insight into perspective error. The analysis and results shown here allow for the proper selection of diagnostic method and analysis approach depending on the flame profile.

2. Methods

2.1. Ballistic Testing

The High-velocity Impact-ignition Testing System (HITS) was used to launch RM projectiles at 1300 m/s into a custom test chamber, shown in Fig. 2 (top). Projectiles were loaded into a 0.410 caliber shotshell with 2.9 g of Alliance Blue Dot™ propellant powder. Two different RM projectile compositions were used: an intermetallic containing Al and Zr, and a thermite containing Al and MoO_3. The powders were consolidated to 10 mm diameter by 10 mm length right circular cylinder projectiles, as pictured in Fig. 2 (bottom). The different RM compositions and impact configurations described below produced different flame profiles during both fragmentation and reaction and provided enough diversity

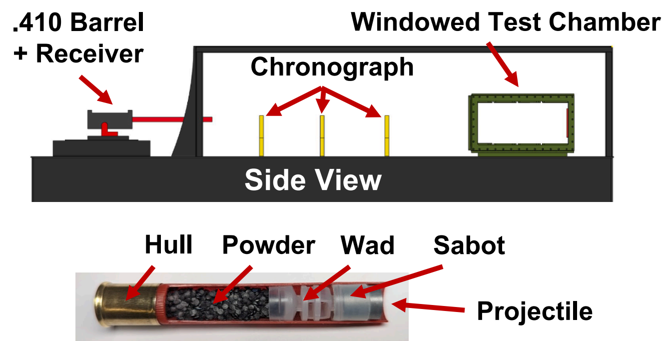

Fig. 2. Top: schematic of the side view of the Texas Tech High-velocity Impact-ignition Testing System (HITS). Projectiles are launched from the barrel and propelled through the chronograph into the windowed test chamber where they impact, ignite, fragment, and react. Bottom: photograph of a 0.410 shotshell loaded with powder, wad, sabot, and projectile to achieve a projectile velocity of 1300 m/s.

in flame symmetry for data analysis based on imaging perspective.

Upon firing, the RM projectile velocity was measured with a Whithner Triggerbox 1000 connected to break-screens (labelled as chronograph in Fig. 2). The projectile then entered a 0.3 x 0.3 x 0.5 m chamber outfitted with viewing windows. Each RM projectile was tested in two chamber configurations: direct impact into a 9.5 mm thick A36 steel plate, and penetration through a 1.5 mm thick A36 steel plate. Different chamber configurations produced different flame profiles by generating different fragmentation patterns. A minimum of three tests were performed for each configuration for repeatability, and a total of 15 tests were conducted.

An Edmund Optics aluminum plate mirror (Stock #46-655) with an $>$ 85 % reflectance was placed above the top window at 45° as shown in Fig. 3. A Phantom v2640 high-speed color camera was mounted on a tripod and aligned to observe both the side and the top view simultaneously. Resolution was set to 512 x 1200 with a frame rate of 12,000 fps and a field of view of 40 x 30 cm, effectively setting spatial resolution at 0.78 mm/pixel. This camera setup allowed simultaneous comparison of two different perspectives upon projectile impact and reaction.

2.2. Thermography

A filter stack containing a triple bandpass filter (450, 532, and 635 nm with bandwidths of 10 nm) and two near-IR short pass filters were attached to the front of a 50 mm Zeiss Interlock lens. This filter stack in combination with the camera's Bayer filter allows for thermographic videos once calibrated. Due to practical considerations of dynamic range and species emissions at combustion temperatures, only the red and green wavelengths (635 nm, 532 nm) were used to calculate temperature.

Calibration requires two steps for single camera systems, a spectral bleed correction and an external standard calibration [2]. Spectral bleed occurs from imperfections in the camera's Bayer filter allowing some red

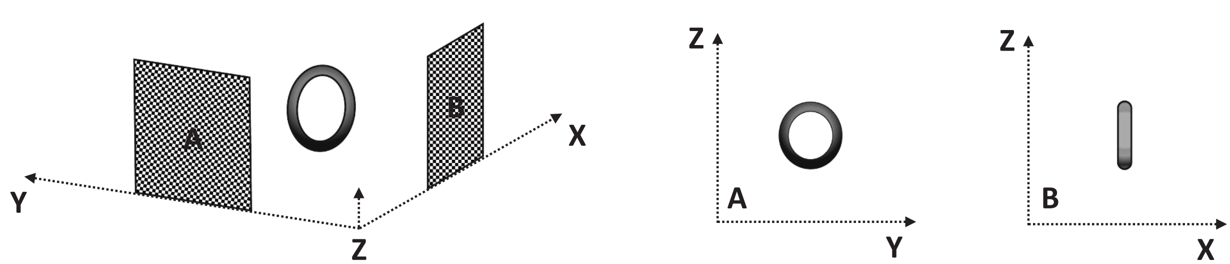

Fig. 1. Perspective projection is demonstrated by looking at a 3-D ring from two 90-degree perspectives. Perspectives A and B show drastically different profiles due to viewing angle and the different appearance is referred to as perspective error.

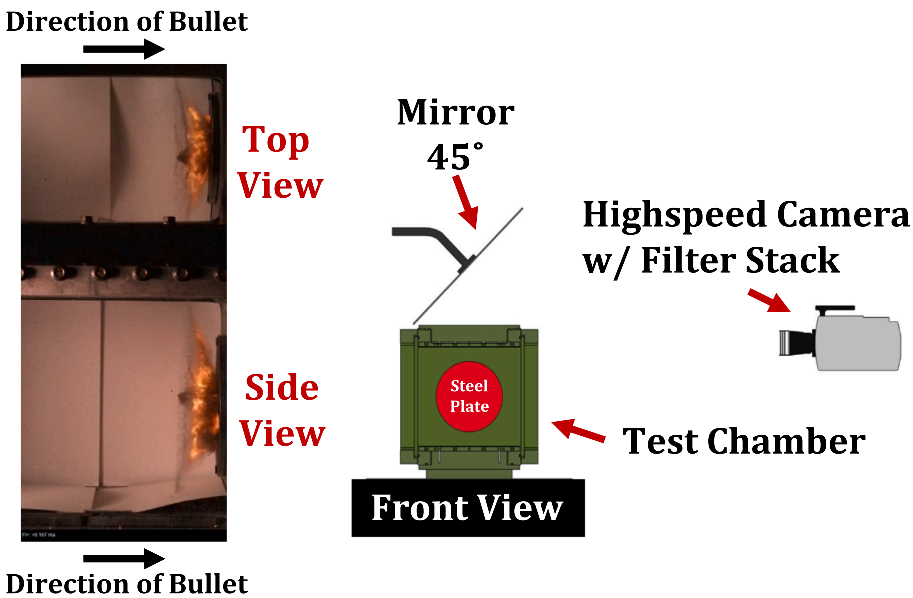

Fig. 3. Schematic of multi-perspective imaging setup. The front view of the windowed test chamber is shown in green with the 9.5 mm thick steel plate positioned at the back of the chamber illustrated in red. The image on the left is a single still frame from the camera with no modifications observing an RM projectile impact event. The still frame image illustrates that the flames and fragmentation can be seen from two perspectives simultaneously.

and green light to reach a pixel only recording blue light. Thorlabs Single-Color Mounted LEDs served to measure the spectral bleed coefficients. The LEDs were lensed with a Thorlabs SM1U adjustable collimator and focused in-frame until the entire camera sensor received an even level of monochromatic light. A short video was recorded, and each pixel was analyzed for spectral bleed-through in relevant channels. This process was repeated for each wavelength of the triple bandpass filter and bleed-through was averaged across all pixels and frames. The second step of calibration used an external standard calibration source (Thorlabs SLS201L tungsten lamp) with a Thorlabs SLS210C collimation lens framed to fill the width of the camera sensor. Video data were captured of the source, and calibration factors averaged over the entire captured area of the collimated beam as detailed in [13]. Final correction factors were applied before analysis as described by McNesby at al. [2].

Separate calibrations were made with and without the 45° mirror and all camera settings were kept the same between calibration and testing. Spectra measured with an Ocean Optics USB4000 Spectrometer both with and without the mirror showed a maximum 2 % difference in intensity between any RGB channel. Otherwise, the mirror acted as a weak neutral density filter (15 % reduction). Weak neutral density filters have no effect on calibration values, so no further corrections were needed. Corrected image intensity data were input of a MATLAB code that processed Eq. (1) for every pixel.

$$\frac{c_2}{\lambda} = -T^{*}\ln\left(\lambda^5 I_b \varepsilon\right) + T^{*}\ln(c_1) \tag{1}$$

In Eq. (1) I_b is the measured intensity of radiation incident upon the imaging plane, ε is emissivity defined as the ratio of real emissive power to the predicted emissive power of a blackbody from Planck's law, c_1 and c_2 are radiation constants ($c_1 = 1.1910 \times 10^8$ W μm^4 m^{-2} sr^{-1} and $c_2 = 1.4388 \times 10^4$ μm K), T is temperature, and λ is wavelength. Pixel intensities at saturation (4095 arbitrary units, a.u., for 12-bit) and lower than 300 a.u. were eliminated from the analysis. An area filter also eliminated data with less than 5 connecting pixels to account for errors in the filter's interpolation algorithm. Eliminated pixels are not included in statistical calculations, however they are included for measurements of symmetry.

2.3. *Optical density*

Separate impact tests were conducted like Brown et al. [14] to measure optical density variations throughout impact induced combustion. Tests were conducted with the same projectiles and experimental setup except without a mirror. Three lasers at wavelengths of 450, 532, and 635 nm (Thorlabs CPS450, Thorlabs CPS532, and Thorlabs CPS635) were positioned perpendicular to the viewing window of the test chamber at approximately 55 mm spacing, as shown in Fig. 4.

A Phantom v2640 high-speed color camera with thermography lensing and a Tiffen 52 mm variable neutral density (ND) filter measured optical density. All three lasers were focused at the camera sensor through the center of the test chamber to measure optical density (OD) variations using Eq. (2).

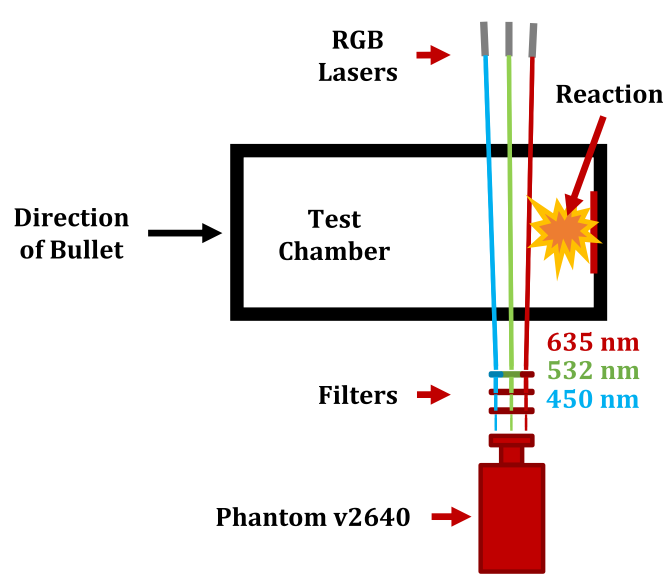

Fig. 4. Schematic of experimental setup for performing optical density measurement. Three lasers at 635, 532, and 450 nm are positioned in three locations to measure optical density throughout combustion and flame spreading.

$$OD = \log_{10}\frac{I}{I_0} \tag{2}$$

In Eq. (2) I_0 is the incident light intensity and I is the measured light intensity [14]. Adjustments were made to the variable ND filter until the camera read an intensity just below saturation (4095 a.u.) for all three lasers. The variable ND filter was set at OD 0.6, and the triple bandpass filter acted as an OD 0.1 ND filter. From Eq. (2), the camera saturated by a factor of 5 without filters in place, thereby increasing the dynamic range of the OD measurements by a factor of OD 0.7. Incident intensity was measured before and after impact to look for reductions caused by particle adhesion and coating the window or window scarring. Incident light change was negligible compared to observed optical density changes, therefore no further corrections were necessary.

3. Results and discussion

Two representative impact events labelled Shot 1 and Shot 2 are compared throughout Section 3. Shot 1 exhibits high degrees of symmetry throughout reaction, whereas Shot 2 is highly asymmetric. To demonstrate the differences in temperature calculations caused by symmetry, every still frame flame profile is grouped into one of three general categories: symmetric, mixed, and asymmetric. Fig. 5 illustrates still frame examples of the differing flame profiles.

Degree of symmetry is quantified by analyzing similarity between top and side perspectives using MATLAB's Structural Similarity Index (SSI) function [15] which compares luminance, contrast, and structure of two images. The SSI processed images are scored between 0 and 1, with 0 indicating no similarity and 1 indicating an exact match. Fig. 6 shows results from the SSI analysis, illustrating the differences in symmetry as a function of time. For this analysis, any frame of video above 0.6 SSI is categorized as symmetric, any frame below 0.3 SSI is categorized as asymmetric, and the intermediate region is categorized as mixed. Therefore, in one test, data can be analyzed respective to the changing SSI classification. The SSI threshold selections are user determined based on visual inspection of the flame profiles and are not intended to be representative of all reactive systems. Instead, these thresholds demonstrate that categorizing analysis by transient

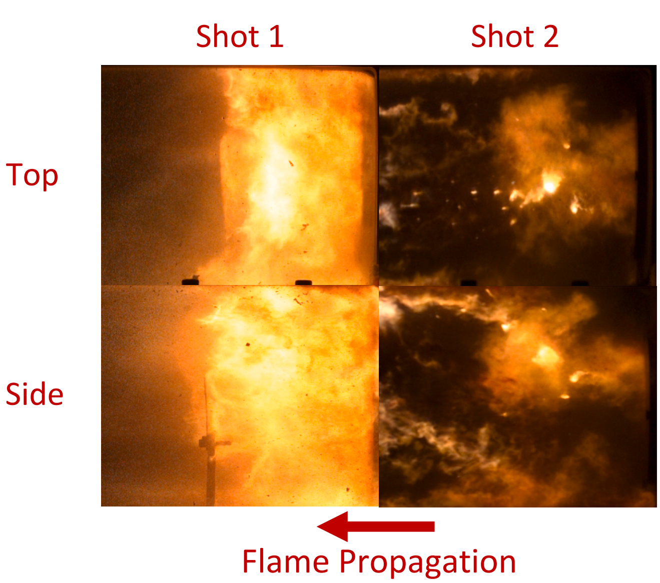

Fig. 5. Still frame images from two different high-speed videos showing representative flame profiles of high (left column) and low (right column) symmetry reactions. Top views are shown in the top row, side views are shown in the bottom row. Asymmetry between the two perspectives can be significant depending on the RM composition and experimental configuration (i.e., penetration or direct impact).

symmetry behavior yields a strong correlation with perspective error. Fig. 6 illustrates the transient nature of flame spreading and that symmetry differs as a function of time, potentially influencing data interpretation.

Symmetric flames exist in high gas-generating, high fragment-dispersion systems. For example, fine powder dispersion produces optically dense symmetric flames. Upon impact, projectiles that fragment into fine powder create a dust explosion rapidly expanding outwards from the point of impact. This expansion exhibits high symmetry which lasts until most of the reaction is complete. After the reaction settles, lingering reactive clumps introduce asymmetric patterns before flames are fully extinguished. Asymmetric flames, on the other hand, contain larger fragments in the debris field, leading to localized regions of high reactivity with distinct and stochastic shapes. Asymmetric flames can exhibit some degree of symmetry during initial impact, fragmentation, and expansion; however, fragments quickly separate and begin to exhibit greater degrees of stochastic asymmetry.

All impact events contain these three flame profiles to some degree, as shown in Fig. 6. Impact events that start symmetric might grow asymmetric over time, or asymmetric flames might disperse into more symmetric flames. Stochastic flame dynamics contribute to the difficulty of optical diagnostics because assumptions for data processing are a function of flame behavior. For example, symmetric flames often start as optically dense clouds that may be modelled by $\boldsymbol{\varepsilon} = 1$ but quickly disperse into optically thin clouds modelled better by $\boldsymbol{\varepsilon} = \frac{1}{\lambda^2}$ [13,14]. Asymmetric flames exhibit optically thin and thick regions simultaneously, preventing any one emissivity assumption from properly characterizing the entire event. These general observations indicate that complex reaction events require additional characterization, such as *in-situ* optical density measurements, to properly contextualize data.

3.1. Symmetric versus asymmetric flame behavior

Still frame images from symmetric and asymmetric profiles are shown in Fig. 7.

To quantify differences in temperature between perspectives, Fig. 8 shows contour plots of the temperature distribution as a function of time for every frame of the dataset in Fig. 7. Top and side views show temperature density where bright, yellow regions are linked to more than 90,000 pixels reporting the indicated temperature.

Fig. 8 (bottom row) illustrates the percent difference in temperature density between top and side perspectives as a function of time, allowing the quantification of potential measurement error based on perspective. For Shot 1, flames expand radially outward from impact and are symmetric throughout most of the combustion event (Fig. 6). Temperature density differences remain relatively small during symmetric expansion (<40 %), with differences likely caused by inherent inhomogeneities. At later stages of flame expansion (i.e., > 7 ms) asymmetries evolve as flames settle throughout the chamber. Temperature density differences between perspectives increase at later times indicating a correlation between flame structure (and subsequent optical density) and measured temperature. Late-time asymmetries present a chance for optical density corrections as the flames are diffuse with elongated profiles depending on flame settling behavior.

For Shot 2, imperfect fragmentation produces spatial asymmetry at the leading edge of the flame profile. During initial expansion (<1 ms), measured symmetry is relatively high because fragmentation has not had time to separate meaningfully. Temperature density differences also remain small during this expansion (<20 %) but quickly spike as fragments experience secondary impact and combustion with the sidewalls. Asymmetry grows rapidly up to 2.5 ms, where temperature density differences spike (>90 %) due to hot spots that are obscured from the top view by the surrounding flame. The spiked differences result from inherent inhomogeneity and should not be corrected. At 6.0 ms the asymmetry persists; the hot spots have fully reacted, but the high

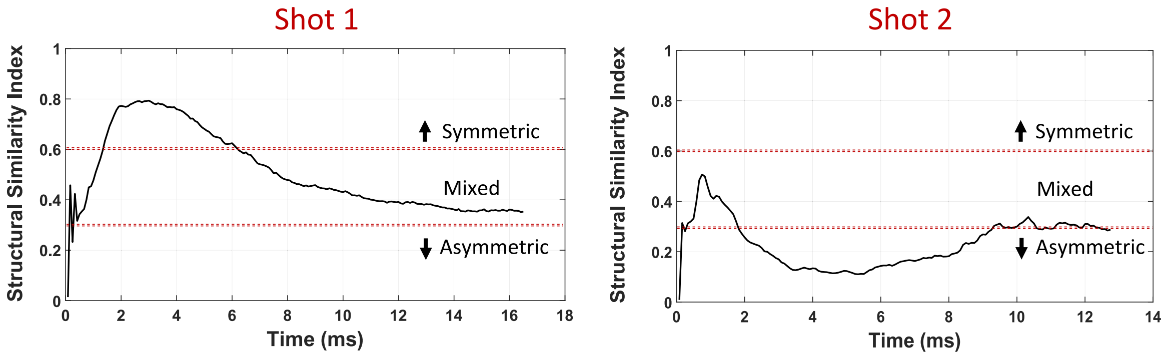

Fig. 6. Results from processing data using MATLAB Structural Similarity Index (SSI) comparing the top and side perspectives of the same impact event. A 1.0 SSI indicates an exact match, 0.0 indicates no similarity. For this analysis, an arbitrary threshold above 0.6 SSI indicates symmetric and below 0.3 SSI indicates asymmetric flame behavior. The region between 0.3 and 0.6 is a mixed regime.

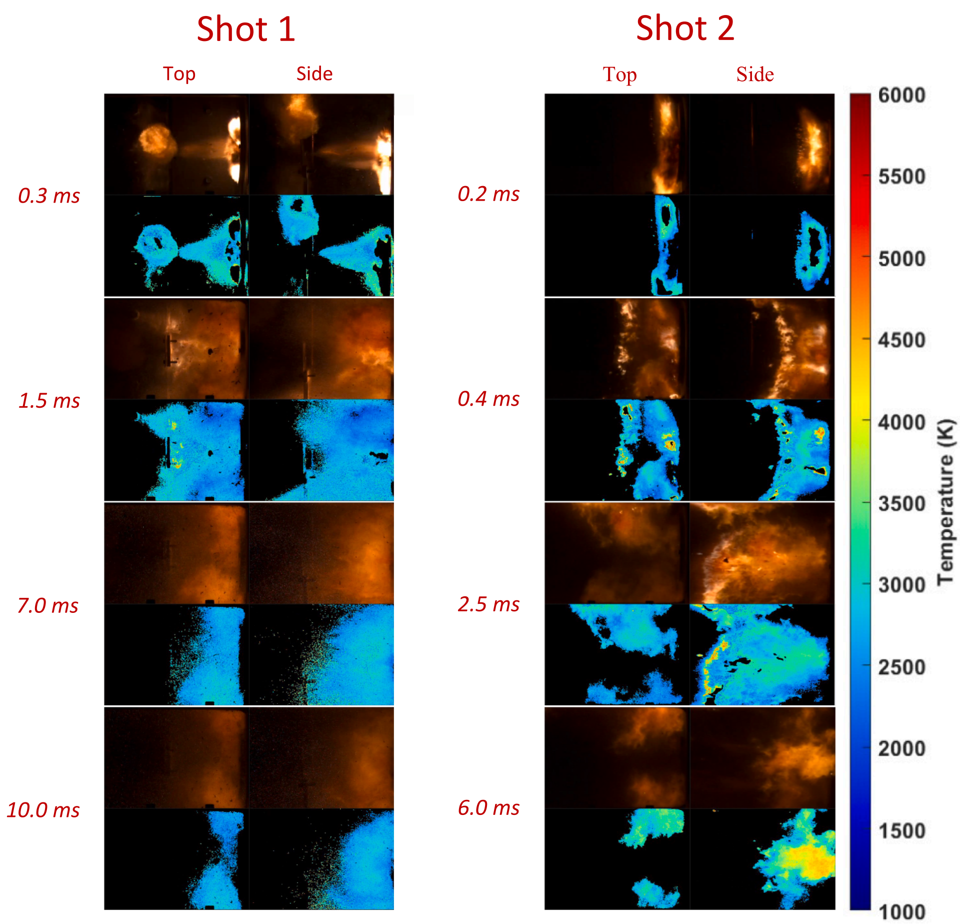

Fig. 7. Still frame images of high-speed thermographic video comparing Shot 1 and Shot 2. Left and right columns correspond to top and side views, respectively. Four total images per timestamp are shown. For each time stamp, top images are un-edited visual data and bottom images are corresponding temperature data calculated applying $\varepsilon = \frac{1}{\lambda^2}$ for both perspectives. The temperature scale bar is provided for reference.

temperature products of reaction are still obscured from the top view. The differences still result from inherent inhomogeneity; however, flame dispersion introduces optical density errors. Differences between perspectives drop after 6.0 ms as the flames diffuse into optically thin clouds, where optical density corrections account for differences between perspectives. Temperature density differences of up to 90 % (Fig. 8) demonstrate the significance of perspective error.

3.2. *Temperature & optical density*

Fig. 8 reports up to 90 % difference in temperature density measurements. Optical density variations caused by the flame's profile contribute to these differences between perspectives. Regions with elongated combustion clouds that have experienced sufficient mixing with neighboring gases are the primary contributor for these errors. Correcting for this optical density bias is considered here.

Optical density influences the emissivity assumption [13]. Highly optically dense flames behave closer to $\varepsilon = 1$ and $\varepsilon = \frac{1}{\lambda}$, and less

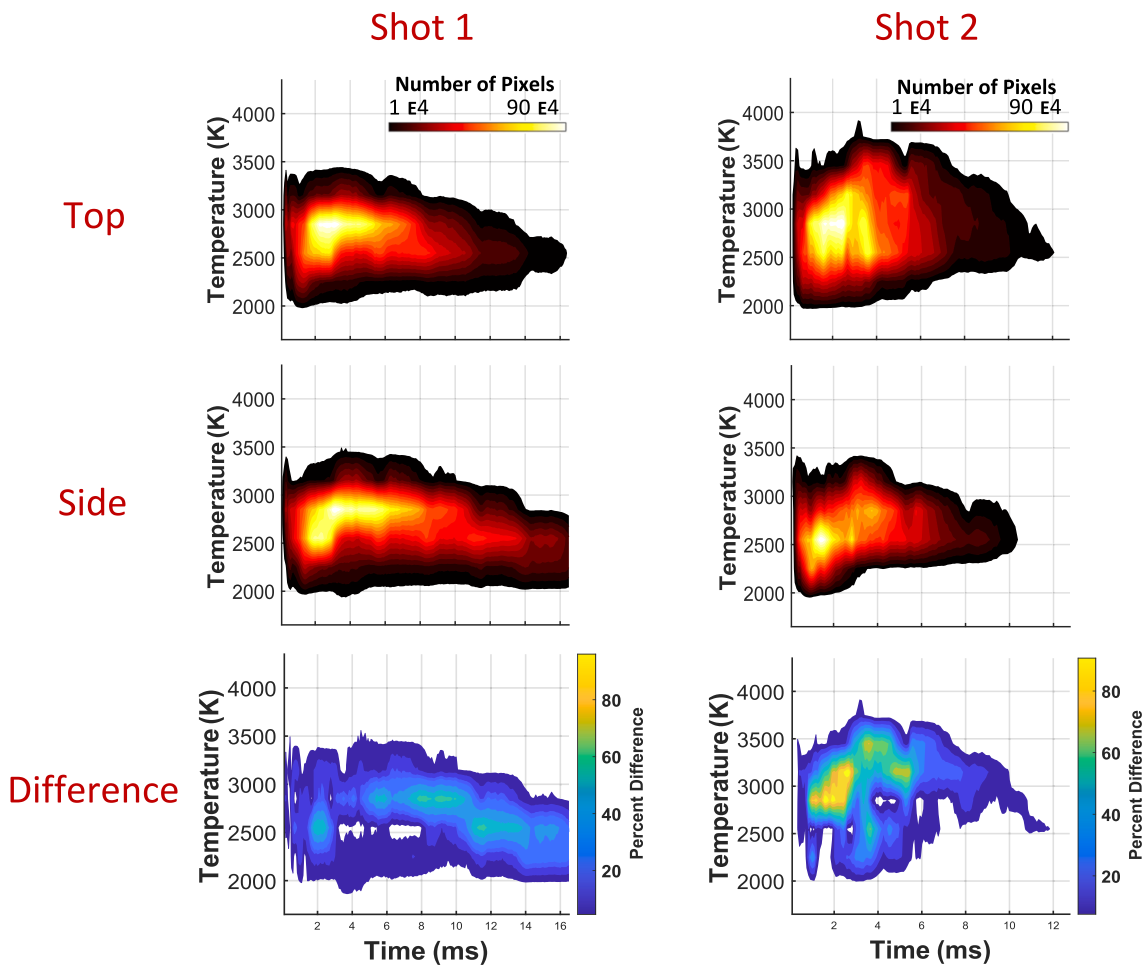

Fig. 8. Contour plots comparing the relative density of pixels reporting indicated temperatures. Black regions indicate < 10,000 pixels measuring the indicated temperature and yellow regions represent > 90,000 pixels measuring the indicated temperature. Data is matched to Figs. 6 and 7. Differences in temperature density distributions are graphically compared in the bottom row of graphs, with blue regions showing little difference between top and side views, and yellow regions showing the greatest difference. (For interpretation of the references to color in this figure legend, the reader is referred to the web version of this article.)

optically dense flames behave closer to $\varepsilon = \frac{1}{\lambda^2}$. Different emissivity assumptions result in large temperature variations (i.e., Eq. (1)), suggesting that the 30 % difference in temperature density during the later stages of reaction (see Fig. 8) could partially be caused by an incorrect emissivity assumption. Corrections for optical density error could be applied as a bias across all temperature values, so different emissivity assumptions are compared using median temperature per frame for simplicity. Fig. 9 compares the percent difference in median

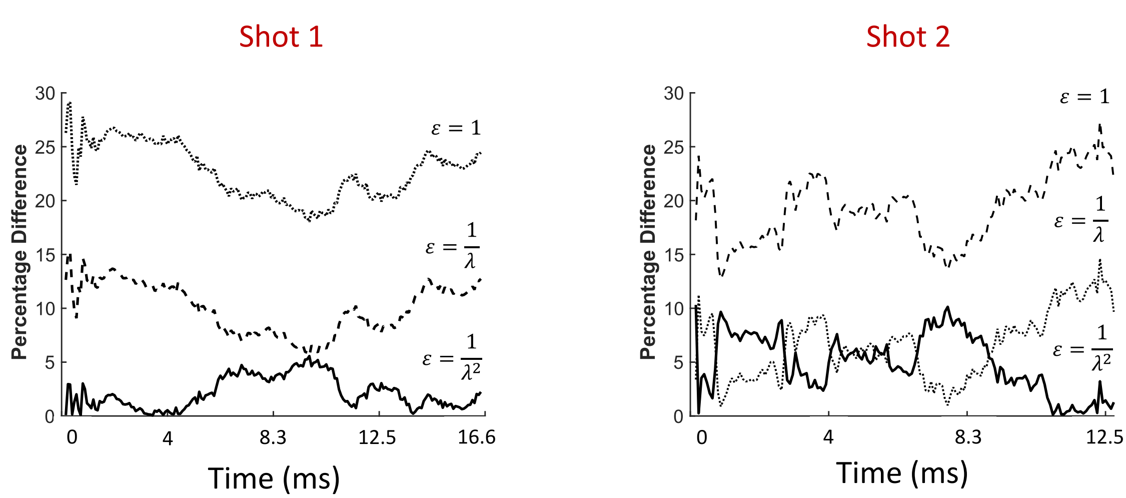

Fig. 9. Percent difference in median temperature between the top and side views. Three different emissivities are plotted for the top view, $\varepsilon = 1$, $\varepsilon = \frac{1}{\lambda}$, and $\varepsilon = \frac{1}{\lambda^2}$, while the side is constant at $\varepsilon = \frac{1}{\lambda^2}$.

temperature and illustrates the effect of changing emissivity assumption between perspectives. By holding the side view emissivity assumption constant at $\varepsilon = \frac{1}{\lambda^2}$ and varying the top view emissivity between $\varepsilon = 1$, $\varepsilon = \frac{1}{\lambda}$, and $\varepsilon = \frac{1}{\lambda^2}$, potential bias from emissivity assumptions can be evaluated.

For Shot 1, if the same emissivity assumption ($\varepsilon = \frac{1}{\lambda^2}$) is used for both perspectives, temperature differences increase in relation to growth in asymmetric effects (Fig. 6). Percentage difference past 4 ms decreases when employing high optical density assumptions ($\varepsilon = 1$, $\varepsilon = \frac{1}{\lambda}$), whereas the percent difference for $\varepsilon = \frac{1}{\lambda^2}$ increases. For this specific reaction, and likely most symmetric flames, the optical density perspective errors may not be large enough to justify corrections. However, for Shot 2 in Fig. 9, as asymmetric dispersions start to diffuse into optically thin mediums, $\varepsilon = \frac{1}{\lambda}$ produces a lower median temperature difference than $\varepsilon = \frac{1}{\lambda^2}$ applied to both perspectives (e.g. at 8 ms). Therefore, the perspective error in asymmetric flames can be reduced through the consideration of the emissivity assumption. Realistically, application of emissivity assumption based on optical density corrections would require *in-situ* knowledge of flame optical density. The median analysis in Fig. 9 could also be extended more rigorously by applying the analysis to individual matched flame groups.

Measurement of optical density is theoretically simple, but practical limitations in spatial resolution of data and difficulties in experimental setup limit comprehensive implementation. Fig. 10 shows a simple measurement of optical density throughout high and low symmetry impact events.

For Shot 1, an optically dense cloud expands from impact blocking light evenly until the cloud has had time to settle, upon which the cloud becomes more transparent. Laser probes closest to the impact anvil (635 nm) experience less fluctuation over time than probes further away (450 nm) due to kinetic expansion no longer occurring in this region of the test chamber. Shot 2 is more stochastic, with each separate wavelength reporting a markedly different optical density. Generally, symmetric flames show more consistent changes in optical density, whereas asymmetric flames produce large variations over short time scales. These measurements demonstrate difficulties in predicting optical density where, depending on the location and time within a reaction, reported values can vary significantly. The ability to spatially measure optical density *in-situ* may enable an emissivity correction to characterize the full flame profile more accurately.

3.3. Temperature difference by symmetry

Figs. 6–8 focused on establishing a link between flame symmetry and median temperature difference based on perspective. Correction for this difference by adjusting emissivity based on optical density (Figs. 9–10) was also discussed. Table 1 is a summary that compares all tests, categorized by flame symmetry or impact type, and tabulates the average percent difference in median temperature as well as the maximum percent difference.

For symmetric flames, any still frame from any impact exceeding the 0.6 SSI threshold is included in the difference calculation. The same procedure is used for asymmetric and mixed flames, respective to thresholds in Section 3. Therefore, the data compiled in Table 1 allows comparing the effects of flame symmetry on data analysis regardless of RM test shot, chemical composition, and impact configuration. Table 1 shows that asymmetric flames, regardless of chemical composition and impact methodology, will exhibit nearly double the percent difference error of symmetric flames. The time and space averaged differences are low overall, with symmetric flames reporting 4 % and asymmetric flames reporting 7 %. As expected, mixed flame differences lie in between symmetric and asymmetric. In Table 1, Max Percent Difference represents the worst-case scenario, the average largest measured difference for each category, and indicates a 13 % difference for symmetric flames and a 27 % difference for asymmetric.

Penetration tests produced more symmetric flames for all reactive projectiles due to more efficient fragmentation. Intermetallic projectiles produced more symmetric flames due to their reactive dependency on fragmentation pattern. The complexity of these systems is high, so it is expected that even highly symmetric flames will exhibit inherent inhomogeneities of > 3 %. Therefore, one perspective of a symmetric flame can reasonably characterize the full reaction. However, as the reaction evolves and asymmetry ensues, temperature differences based on perspective can increase. Results summarized in Table 1 indicate dominantly asymmetric flames are less reasonably expected to produce the same result between different perspectives.

Table 1
Every still frame from all tests is analyzed and compiled by flame profile as symmetric, asymmetric, or mixed (as defined in Section 3). The maximum and average percentage difference of median temperature are calculated for each category. Details on the projectile and experimental configuration are also included.

Flame Type	Max Percent Difference	Avg. Percent Difference
Symmetric	13	4
Asymmetric	27	7
Mixed	20	6
Projectile Impact	**Max Percent Difference**	**Avg. Percent Difference**
Intermetallic Impact	8	4
Intermetallic Penetration	18	5
Thermite Impact	25	7
Thermite Penetration	8	6

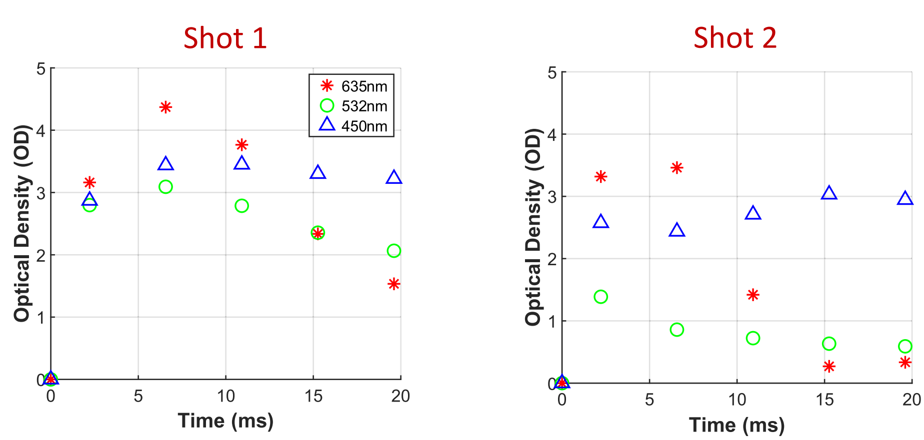

Fig. 10. Measured optical density for the three wavelengths shown in Fig. 5 within the chamber and throughout an impact induced reaction event.

4. Conclusion

This study analyzed the influence of imaging perspective on transient, two-dimensional emission data from impact induced reactive material (RM) combustion. The RM composition and the test configuration were varied to intentionally produce different flame profiles that were analyzed using thermography from two perspectives simultaneously. The goal was to quantify perspective error for temperature measurements of macro-scale fireball flame profiles.

Symmetric, asymmetric, and mixed flame profiles were defined by a structural similarity index (SSI) and thresholds were applied to distinguish between data sets. For any given test shot, the still frame data categorized by SSI is highly transient, such that a test shot might produce all three categorizations for a finite duration throughout the test. Regardless of RM test shot, chemical composition, or impact configuration, data corresponding to highly symmetric flames typically result from finer fragmentation dispersion and burn like an optically dense dust cloud that is less dependent on viewing perspective. In contrast, asymmetric flames produce larger fragments that burn as localized clumps. Correcting temperature differences between perspectives in asymmetric flames was possible by adjusting the emissivity assumption based on the optical density measured in a specific region.

Asymmetric flames when measured from multiple perspectives showed on average a 7 % difference in median temperatures, with maximum differences up to 27 %. Symmetric flames showed greater consistency with a 4 % difference in median temperatures and a maximum of 13 %. Overall, thermography from a single perspective can more accurately characterize symmetric flames. Asymmetric flames exhibit large potential perspective error and must be analyzed accordingly.

CRediT authorship contribution statement

Colton Cagle: Writing – original draft, Methodology, Investigation, Formal analysis, Data curation, Conceptualization. **Michelle Pantoya:** Writing – review & editing, Supervision, Project administration, Methodology, Funding acquisition, Conceptualization.

Declaration of competing interest

The authors declare no competing interests.

Data availability

Data will be made available on request.

Acknowledgements

The authors are thankful for support from ONR: N00014-19-1-2006 as well as STEM grants from ONR: N00014-21-1-2519 and from DOE: DE-NA0003988. Mr. Charles Luke Croessmann and Mr. Frank Muniz from Texas Tech University are gratefully acknowledged for experimental assistance.

References

[1] A. Araújo, Multi-spectral pyrometry—a Review, Meas. Sci. Technol. 28 (8) (2017) 082002.
[2] K. McNesby, S. Dean, R. Benjamin, J. Grant, J. Anderson, J.M. Densmore, Imaging pyrometry for most color cameras using a triple pass filter, Rev. Sci. Instrum. 92 (6) (2021) 063102.
[3] J.M. Densmore, M.M. Biss, K.L. McNesby, B.E. Homan, High-speed digital color imaging pyrometry, Appl. Opt. 50 (17) (2011) 2659.
[4] M. Kulichenko, J.S. Smith, B. Nebgen, Y.W. Li, N. Fedik, A.I. Boldyrev, N. Lubbers, K. Barros, S. Tretiak, The rise of neural networks for materials and chemical dynamics, J. Phys. Chem. Lett. 12 (26) (2021) 6227–6243.
[5] D.L. Blunck, Review: applications of infrared thermography for studying flows with participating media, Exp. Therm Fluid Sci. 130 (2022) 110502.
[6] O. Faugeras, Q.-T. Luong, The geometry of multiple images: the laws that govern the formation of multiple images of a scene and some of their applications, The MIT Press, Cambridge, Massachusetts, 2001.
[7] A.P. Tafti, A.B. Kirkpatrick, Z. Alavi, H.A. Owen, Z. Yu, Recent advances in 3D SEM surface reconstruction, Micron 78 (2015) 54–66.
[8] N. Yan, Y. Mei, L. Xu, H. Yu, B. Sun, Z. Wang, Y. Chen, Deep learning on image stitching with multi-viewpoint images: a survey, Neural Process Lett 55 (2023) 3863–3898.
[9] C. Yuan, H. Niemann, Neural networks for the recognition and pose estimation of 3D objects from a single 2D perspective view, Image Vis. Comput. 19 (2001) 9–10.
[10] S. H. Fischer and M. C. Grubelich, Theoretical energy release of thermites, intermetallics, and combustible metals, Sandia National Laboratory Report No. *SAND-98-1176C* (1998).
[11] C.L. Croessmann, C. Cagle, P. Dube, J. Abraham, I. Altman, M.L. Pantoya, Thermite and intermetallic projectiles examined experimentally in air and inert gas environments, J. Appl. Phys. 7 (2022) 175904.
[12] W. K. Lewis, N. G. Glumac, E. G. Yukihara, Time-dependent temperature measurements in post-detonation combustion: current state-of-the-art methods and emerging technologies, *United States: Np.*, AD1006208, 2016. Web.
[13] C. Woodruff, S.W. Dean, C. Cagle, C.L. Croessmann, M.l. Pantoya, Comparing pyrometry and thermography in ballistic impact experiments, Measurement 189 (2022) 110488.
[14] A. D. Brown, M. Gomez, T. R. Meyer, S. F. Son, D. R. Guildenbecher, Imaging Pyrometry and Optical Depth Measurements in Explosive Fireballs Using High-Speed Imaging, Proceedings of the American Institute of Aeronautics and Astronautics (AIAA), AIAA-2022-1311 Session: Advanced Flow Visualization I, *AIAA SCITECH 2022 Forum*, 2022.
[15] Z. Wang, A.C. Bovik, H.R. Sheikh, E.P. Simoncelli, Image quality assessment: from error visibility to structural similarity, IEEE Trans. Image Process. 13 (4) (2004) 600–612.